CHEMISTRY OF MATERIALS

Article

pubs.acs.org/cm

Ru-Cluster-Modified Ni Surface Defects toward Selective Bond Breaking between C−O and C−C

Hao Chen,[†] Shan He,[*,†] Xingzhong Cao, Shitong Zhang,[†] Ming Xu,[†] Min Pu,[†] Dangsheng Su,[*,§] Min Wei,[*,†] David G. Evans,[†] and Xue Duan[†]

[†]State Key Laboratory of Chemical Resource Engineering, Beijing University of Chemical Technology, Beijing 100029, P. R. China
Institute of High Energy Physics, Chinese Academy of Sciences, Beijing 100049, P. R. China

[§]Shenyang National Laboratory of Materials Science, Institute of Metal Research, Chinese Academy of Sciences, Shenyang 110016, P. R. China

Supporting Information

ABSTRACT: For catalytic processes involving multiple reaction pathways such as the ethanol steam reforming (ESR), tailoring the active site structure of catalysts to achieve the desired catalytic selectivity is of vital importance and remains a challenge. Here, we report a heterogeneous Ru−Ni catalyst by anchoring Ru clusters onto the defect sites of Ni nanoparticles. The resulting strained Ru−Ni interface shows a high activity toward the C−C bond cleavage that is essentially required for hydrogen production via ESR. The C−O bond rupture in the side reaction (methanation) is significantly inhibited. This results in an extremely high H_2 yield of 4.2 mol_{H_2}/mol_{EtOH} at 350 °C, superior to the previously reported ESR catalysts working at medium-low temperature (300−500 °C). An experimental-computational combination study verifies that the conversion of Ni surface defects to the Ru−Ni interface plays a decisive role in the remarkably improved H_2 yield. This work demonstrates an effective strategy to largely enhance the bond-breaking selectivity via tuning the active site structure at the catalyst surface/interface.

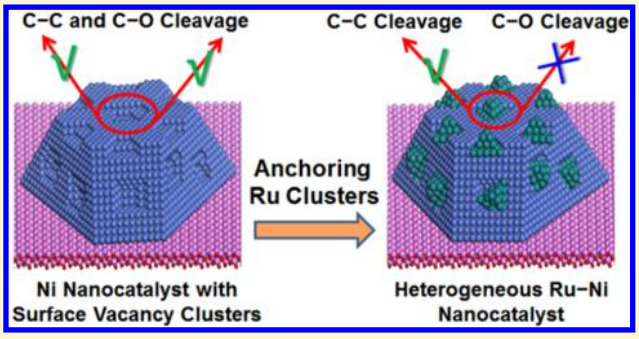

INTRODUCTION

The defect structure on the metal catalyst surface, with a large density of low-coordinated atoms and a higher-lying d state, normally enables enhanced binding of reactant molecules and serves as the active sites for heterogeneous catalysis processes.[1−5] Therefore, the surface defects may dominate the reactivity of catalysts, and great efforts have been made to develop novel metal catalysts with abundant and controllable surface defects.[6−8] However, for catalytic processes involving multiple reaction pathways, knowledge concerning the influence of the defect structure on catalytic selectivity is still lacking, and how to achieve largely improved selectivity via tuning the defect structure remains a challenge. Such detailed information is valuable in rational design and preparation of new catalysts with desired selectivity.

Steam reforming of ethanol (ESR) as a multiple-pathway reaction, derived from the development of biomass technology, is widely regarded as a promising approach for hydrogen production; the key point is the catalyst design and exploration so as to achieve a high yield of H_2 at a mild reaction temperature (see the introduction of ESR in the Supporting Information).[9,10] Supported Ni-based catalysts have shown prominent catalytic activity toward ESR at medium-low reaction temperatures (300−500 °C), due to their strong capability to break a σ C−C bond.[10,11] However, their selectivity to H_2 is rather restricted owing to the facile occurrence of the C−O π-bond rupture (as the rate-determining step for the side reaction methanation[12,13]), leading to a remarkably decreased H_2 yield.[14−17] As a result, the requirements for ESR catalysts must simultaneously satisfy the facilitation of C−C bond cleavage and inhibition of the C−O π-bond rupture at low temperatures. Notably, both C−C and C−O bond cleavage are structure-sensitive to the metal surface structure with high-lying d states (e.g., surface defects);[18−20] a rational design of supported Ni-based catalysts with a tunable surface structure is thus of vital importance to enhance the bond-breaking selectivity between C−O and C−C bonds.

Herein, supported Ni nanoparticles with various concentrations of surface defects were first prepared on the basis of an in situ topotactic reduction of the NiAl−hydrotalcite precursor and subsequently an annealing treatment. Ni surface defects as active sites promote C−C and C−O bond cleavage simultaneously in ESR, but C−O bond cleavage displays a much stronger surface-defect-dependence. To inhibit the C−O bond rupture, we modify the surface defects of Ni nanoparticles by anchoring Ru clusters; the obtained catalyst with a strained

Received: May 4, 2016
Revised: June 5, 2016
Published: June 13, 2016

DOI: 10.1021/acs.chemmater.6b01784
Chem. Mater. 2016, 28, 4751−4761

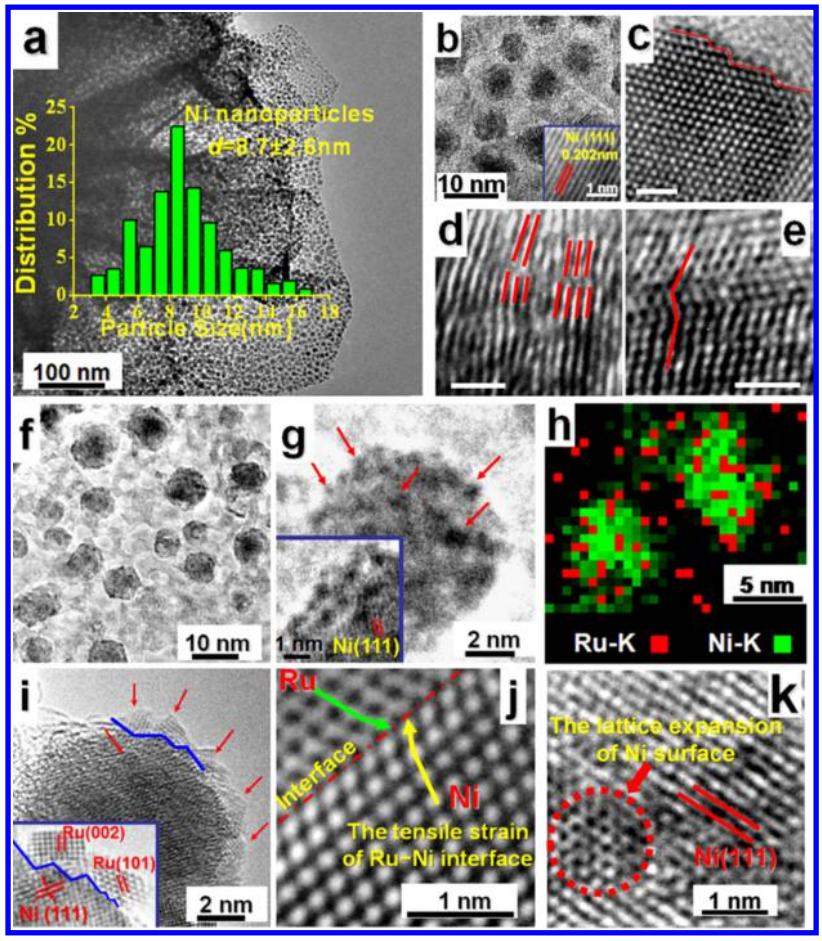

Figure 1. HRTEM images of Ni/H−Al_2O_3: (a) an overall image, (b) one nanoflake with embedded Ni nanoparticles (inset: lattice fringes of Ni nanoparticle), (c−e) a single Ni nanoparticle (the scale bar is 1 nm). HRTEM images of $Ru_{0.8}$−Ni/H−Al_2O_3: (f) an overall image, (g) a single Ru−Ni nanoparticle (inset: a large magnification image), (h) EDS mapping of Ni (green, Ni-k) and Ru (red, Ru−K) elements for two selected Ru−Ni nanoparticles, (i) the cross-sectional image of one Ru−Ni nanoparticle (inset: a large magnification image), (j) the image of the Ru−Ni interface, (k) the top-view image of one Ru cluster embedded onto the surface of a Ni nanoparticle.

Ru−Ni interface is highly active for H_2 production via ESR. An experimental-computational combination study demonstrates that the blocking of Ni surface defects via Ru anchoring remarkably inhibits the C−O bond rupture and the resulting methanation; while Ru−Ni interfacial sites effectively promote C−C bond cleavage and consequently enhance a H_2 yield, due to a desirable modulation of the metal d-band center position to a moderate energy state. It is expected that the study on bond-breaking selectivity over the metal−metal interface can be extended to other multiple reaction systems with structure sensitive catalysis.

RESULTS AND DISCUSSION

Structural and Morphological Characterizations. The supported Ni nanoparticles with a high concentration of surface defects, derived from a hierarchical NiAl−LDH precursor, were prepared by a method reported by our group (denoted as Ni/H−Al_2O_3),[21] with a more precise control over the reduction conditions in this work. HRTEM images reveal the well-dispersed Ni nanoparticles (8.7 ± 2.6 nm) on the nanoflake substrate (Figure 1a and 1b). As shown in Figure 1c−e, steps, stacking faults, and dislocations on Ni nanoparticles, recognized as highly energetic sites,[22] are observed in HRTEM images. Moreover, by an annealing treatment of Ni/H−Al_2O_3 at 500 and 550 °C, respectively, Ni_{A500}/H−Al_2O_3 and Ni_{A550}/H−Al_2O_3 were obtained to tune the concentration of Ni surface defects; the resulting two samples inherit the original morphology of Ni/H−Al_2O_3, with a close average size of Ni nanoparticles (Figure S1a−d: 9.0 ± 2.5 and 9.2 ± 2.7 nm, respectively).

In order to modify the structure of the Ni surface defect, Ru clusters (0.85 wt %) were anchored onto the surface of Ni nanoparticles in Ni/H−Al_2O_3 via a homogeneous deposition−precipitation (HDP) of Ru species followed by a reduction process (denoted as $Ru_{0.8}$−Ni/H−Al_2O_3). The TEM image (Figure 1f) displays that the as-prepared $Ru_{0.8}$−Ni/H−Al_2O_3 also inherits the original morphology of Ni/H−Al_2O_3, with a similar average particle size (8.4 ± 3.0 nm). The HRTEM image (Figure 1g) and EDS mapping (Figure 1h) show well-dispersed Ru clusters with a uniform size distribution (1.1 ± 0.4 nm) on the surface of the Ni nanoparticle. Figure 1i displays the cross-sectional image of one single Ru−Ni nanoparticle: the lattice fringe of 0.202 nm corresponds to the {111} plane of the cubic Ni phase; while those of 0.206 and 0.213 nm are indexed to the {101} and {002} planes of the hexagonal Ru phase (the inset of Figure 1i). This demonstrates the segregation of Ru clusters rather than the formation of the Ru−Ni alloy on the Ni surface. More interestingly, it is found in Figure 1i that the resulting Ru clusters selectively grow on the low-coordinated site of Ni nanoparticle. A tensile lattice fringe in the atomic

DOI: 10.1021/acs.chemmater.6b01784
Chem. Mater. 2016, 28, 4751−4761

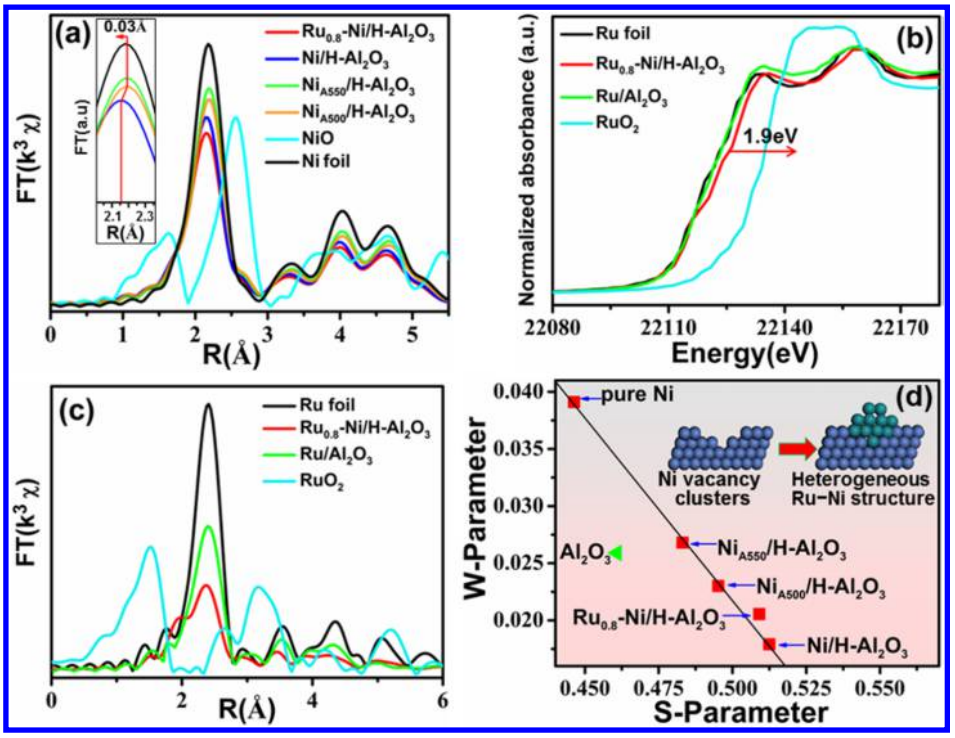

Figure 2. (a) Fourier-transform EXAFS spectra at the Ni K-edge for Ni/H−Al_2O_3, Ni_{A500}/H−Al_2O_3, Ni_{A550}/H−Al_2O_3, and $Ru_{0.8}$−Ni/H−Al_2O_3 (inset: enlarged FT EXAFS spectra on the Ni−Ni interatomic distance for the Ni foil, Ni_{A550}/H−Al_2O_3, Ni_{A500}/H−Al_2O_3, and Ni/H−Al_2O_3). (b) Normalized XANES spectra at the Ru K-edge for $Ru_{0.8}$−Ni/H−Al_2O_3 and Ru/Al_2O_3. (c) Fourier-transform EXAFS spectra at the Ru K-edge for $Ru_{0.8}$−Ni/H−Al_2O_3 and Ru/Al_2O_3. (d) S- and W-parameter correlation (S−W plot) obtained from coincidence Doppler broadening (CDB) for Ni/H−Al_2O_3, Ni_{A500}/H−Al_2O_3, Ni_{A550}/H−Al_2O_3, $Ru_{0.8}$−Ni/H−Al_2O_3, pure Ni, and pristine Al_2O_3.

layer at the Ru−Ni interface is observed (Figure 1j), accompanied by the lattice expansion of the Ni surface (Figure 1k), which is possibly attributed to formation of the Ru−Ni bond with an interfacial strain. The anchoring of Ru clusters onto the surface defects of Ni nanoparticles can be understood from the viewpoint of surface energy and bond dissociation energy (see the detailed discussion in the SI). As a reference sample, Ru/Al_2O_3 (Figure S1e−f) was prepared by the traditional deposition method and was characterized by a small average size with narrow distribution (1.7 ± 0.57 nm). In addition, the specific surface area and chemical compositions of Ni/H−Al_2O_3, Ni_{A500}/H−Al_2O_3, Ni_{A550}/H−Al_2O_3, $Ru_{0.8}$−Ni/H−Al_2O_3, and Ru/Al_2O_3 are listed in Table S1.

We use EXAFS spectroscopy to reveal the detailed structure of various samples. The refined local Ni atomic arrangements were examined in R space (Figure 2a and Table 1); Fourier-transform (FT) EXAFS spectra at Ni K-edge for Ni/H−Al_2O_3, Ni_{A500}/H−Al_2O_3, Ni_{A550}/H−Al_2O_3, and $Ru_{0.8}$−Ni/H−Al_2O_3 show a common dominant peak corresponding to the first Ni−Ni shell in metallic Ni. For the three supported Ni samples, the Ni−Ni coordination number increases in the following order: Ni/H−Al_2O_3 (8.8) < Ni_{A500}/H−Al_2O_3 (9.6) < Ni_{A550}/H−Al_2O_3 (10.0); while the Debye−Waller factor of the Ni−Ni shell displays an inverse tendency: Ni/H−Al_2O_3 (0.008) > Ni_{A500}/H−Al_2O_3 (0.006) > Ni $_{A550}$/H−Al_2O_3 (0.004). The largest Debye−Waller factor but lowest coordination number and shortest Ni−Ni distance (Figure 2a) are observed for Ni/H−Al_2O_3, suggesting a severely distorted fcc Ni environment associated with abundant Ni defects. An annealing treatment of Ni/H−Al_2O_3 leads to an increased Ni−Ni coordination number but a decreased Debye−Waller factor, indicating a better crystallinity and less structural distortion for Ni_{A500}/H−Al_2O_3 and Ni_{A550}/H−Al_2O_3 samples. Interestingly, although $Ru_{0.8}$−Ni/H−Al_2O_3 and Ni/H−Al_2O_3 show close average particle size (8.4 nm vs 8.7 nm), the former sample shows a slightly smaller Ni−Ni coordination number (8.1) than the latter one (8.8). This may indicate the formation of interfacial Ni−Ru coordination, which will be verified by the following EXAFS spectra at the Ru K-edge.

Table 1. EXAFS Fitting Parameters at the Ni K-Edge and the Ru K-Edge for Various Samples

sample	shell	N[a]	R[b] (Å)	$\Delta\sigma^{2}$[c] (Å^2)	ΔE[d] (eV)
Ni foil	Ni−Ni	12.0	2.50		
Ni/H−Al_2O_3	Ni−Ni	8.8	2.47	0.008	2.8
Ni_{A500}/H−Al_2O_3	Ni−Ni	9.6	2.49	0.006	2.5
Ni_{A550}/H−Al_2O_3	Ni−Ni	10.0	2.49	0.004	2.1
$Ru_{0.8}$−Ni/H−Al_2O_3	Ni−Ni	8.1	2.48	0.007	1.8
	Ni−Ru				
Ru foil	Ru−Ru	12.0	2.68		
Ru/Al_2O_3	Ru−Ru	7.1	2.67	0.004	−3.8
$Ru_{0.8}$−Ni/H−Al_2O_3	Ru−Ru	4.0	2.65	0.006	−4.3
	Ru−Ni	2.1	2.58	0.007	−2.5

[a]Coordination number. [b]Bonding distance. [c]Debye−Waller factor. [d]Inner potential shift. Error bounds (accuracies) characterizing the structural parameters obtained by EXAFS spectroscopy are estimated as follows: ±20% for N and ±0.02 Å for R.

The normalized Ru K-edge XANES spectra of $Ru_{0.8}$−Ni/H−Al_2O_3 and Ru/Al_2O_3 (Figure 2b) are rather close to the Ru foil than RuO_2, suggesting the metallic state of Ru in these two samples. Importantly, a slight shift (∼1.9 eV) of the absorption edge toward high photon energy relative to the Ru foil is observed, which indicates the existence of Ru−Ni interaction/

DOI: 10.1021/acs.chemmater.6b01784
Chem. Mater. 2016, 28, 4751−4761

Table 2. Positron Lifetimes, Relative Intensities, and Parameters *S* Value for Various Samples

sample	τ_1 (ps)	τ_2 (ps)	τ_3(ns)	I_1 (%)	I_2 (%)	I_3 (%)	I_2/I_1	S
pristine Al_2O_3	253.3	583.4	2.44	64.7	30.4	4.93	0.47	0.4608
$Ni/H-Al_2O_3$	213.9	424.8	2.36	40.5	56.9	2.63	1.40	0.5125
$Ni_{A500}/H-Al_2O_3$	208.7	417.7	2.38	48.1	49.2	2.73	1.02	0.4952
$Ni_{A550}/H-Al_2O_3$	210.4	412.6	2.41	54.1	42.9	3.01	0.79	0.4831
$Ru_{0.8}-Ni/H-Al_2O_3$	209.1	381.5	2.34	42.3	55.0	2.72	1.30	0.5091

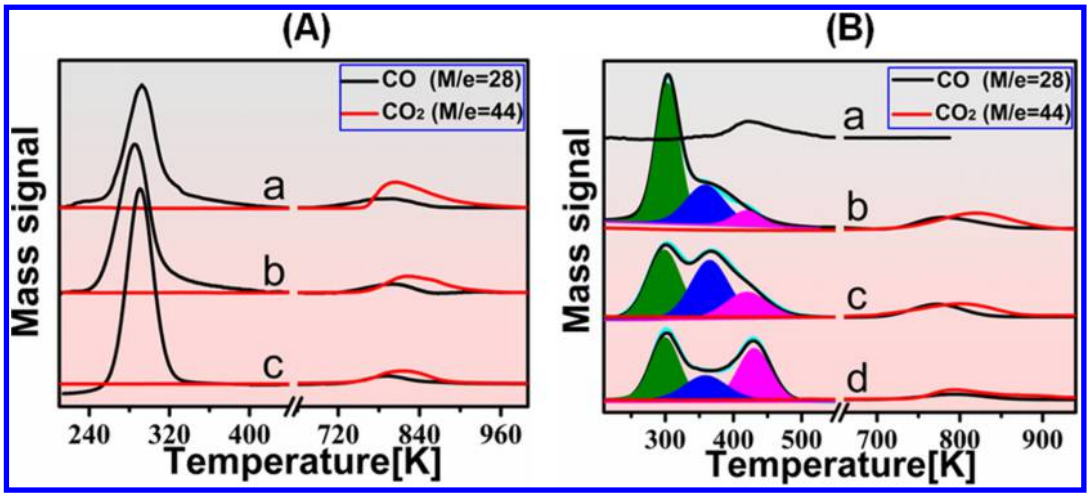

Figure 3. (A) Temperature-programmed desorption curves of CO pulse saturated adsorption at 200 K: (a) $Ni/H-Al_2O_3$, (b) $Ni_{A500}/H-Al_2O_3$, (c) $Ni_{A550}/H-Al_2O_3$. (B) TPD curves of CO pulse saturated adsorption at 200 K: (a) Ru/Al_2O_3, (b) $Ru_{0.4}-Ni/H-Al_2O_3$, (c) $Ru_{0.8}-Ni/H-Al_2O_3$, (d) $Ru_{2.5}-Ni/H-Al_2O_3$. Green area: CO desorption from the weak adsorption site of Ni; blue area: CO desorption from the Ru−Ni interface site; magenta area: CO desorption from the Ru site.

coordination in the $Ru_{0.8}-Ni/H-Al_2O_3$ and a resulting d-electron excursion from the Ru atom to the Ni atom.[23,24] The coordination number of the Ru−Ni bond (Figure 2c and Table 1) is 2.1 in $Ru_{0.8}-Ni/H-Al_2O_3$, smaller than that of the Ru−Ru bond (4.0), further confirming the existence of Ru−Ni interfacial coordination.

The Defect Structure of Monometallic and Bimetallic Samples. We use coincidence Doppler broadening (CDB) and positron lifetime of positron annihilation spectroscopy (PAS) to assess the defects structure of various catalysts; the positrons as probe are trapped by defects with different electron density or/and positron affinity, showing different annihilation characteristics.[25] The electronic and chemical environment of positron trapping sites are usually identified by the parameters S and W obtained from CDB spectrum (see the Experimental Section).[26−28] In this work, the plot of S vs W for $Ni/H-Al_2O_3$, $Ni_{A500}/H-Al_2O_3$, $Ni_{A550}/H-Al_2O_3$, $Ru_{0.8}-Ni/H-Al_2O_3$, pure Ni, and pristine Al_2O_3 is shown in Figure 2d, in which the three Ni-based samples, $Ru_{0.8}-Ni/H-Al_2O_3$, and pure Ni are distributed along a straight line, indicating that the sites of positron annihilation in these samples are mainly associated with Ni vacancy-type defect (e.g., monovacancy and vacancy clusters).[29,30] Notably, the value of parameter S in the three supported Ni samples decreases in the following order (Figure 2d and Table 2): $Ni/H-Al_2O_3$ (0.5125) > $Ni_{A500}/H-Al_2O_3$ (0.4952) > $Ni_{A550}/H-Al_2O_3$ (0.4831). Since parameter S value enhances monotonically with the increase of the defect concentration,[27,28] the significant change in this work indicates a decrease in the concentration of Ni vacancy clusters after the annealing process. This is in agreement with the results of EXAFS.

Positron lifetime contains the information about the size, type, and relative density of defects in a solid.[25] In Table 2, the components τ_3 and τ_1 are attributed to the large voids and small size defects (e.g., monovacancies) in the bulk section of nanoparticles, respectively; the component τ_2 is ascribed to large size defects (e.g., vacancy clusters containing step sites, as shown in Figure 2d) which are typically formed on the surface and interface of nanoparticles.[25,31−33] Moreover, their relative concentration can be reflected by the intensity (I) of the positron lifetime.[31−33] Generally, the relatively larger size defect as a deep electron trap has a lower average electron density and a consequently increased τ_2; while the relatively smaller size defect shows a reverse tendency.[25,32] Compared with $Ni/H-Al_2O_3$, $Ru_{0.8}-Ni/H-Al_2O_3$ shows a considerably decreased τ_2 (381.5 vs 424.8 ps) associated with the modification of Ni vacancy clusters by Ru clusters. The anchoring Ru clusters onto Ni vacancy clusters leads to the formation of interfacial Ru−Ni coordination (as shown in Figure 2d), which enhances the average electron density around Ni vacancy clusters; while the original Ni vacancy clusters as deep electron traps are replaced by the Ru−Ni interface defects as shallow electron traps in $Ru_{0.8}-Ni/H-Al_2O_3$. This thus results in a decrease in τ_2 for $Ru_{0.8}-Ni/H-Al_2O_3$.

In addition, the I_2/I_1 ratio represents the relative concentration proportion of large size defects to small size defects, which is listed in Table 2. $Ru_{0.8}-Ni/H-Al_2O_3$ and $Ni/H-Al_2O_3$ show a close I_2/I_1 ratio, which is likely attributed to newly formed Ru−Ni interface defects with comparable concentration of original Ni vacancy clusters. Compared with $Ni/H-Al_2O_3$, both $Ni_{A500}/H-Al_2O_3$ and $Ni_{A550}/H-Al_2O_3$ do not show a significant change in τ_2, but the I_2/I_1 ratio remarkably decreases with the increase of annealing temper-

DOI: 10.1021/acs.chemmater.6b01784
Chem. Mater. 2016, 28, 4751−4761

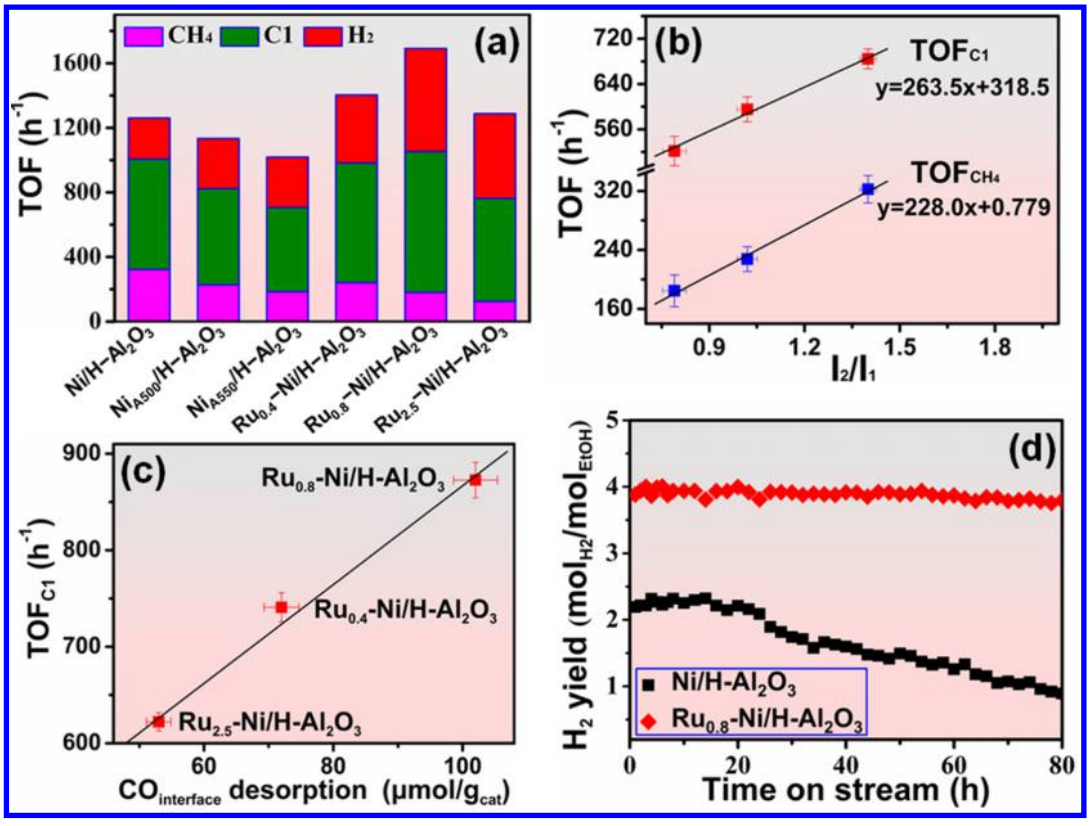

Figure 4. (a) TOF_{C_1}, TOF_{CH_4}, and TOF_{H_2} of various catalysts. (b) Correlation of TOF_{C_1} and TOF_{CH_4} as a function of the I_2/I_1 ratio for Ni/H−Al_2O_3, Ni_{A500}/H−Al_2O_3, and Ni_{A550}/H−Al_2O_3, respectively. (c) Relationship between TOF_{C_1} and the Ru−Ni interface site (represented as $CO_{interface}$ desorption capacity) for $Ru_{0.4}$−Ni/H−Al_2O_3, $Ru_{0.8}$−Ni/H−Al_2O_3, and $Ru_{2.5}$−Ni/H−Al_2O_3. (d) Plots of a H_2 yield vs reaction time at 350 °C for Ni/H−Al_2O_3 and $Ru_{0.8}$−Ni/H−Al_2O_3, respectively.

ature, indicating a largely reduced concentration of Ni vacancy clusters without obvious variation in defect property.

The Surface Structure of Monometallic and Bimetallic Samples. CO−TPD based on low-temperature CO pulse titration was carried out to investigate the surface structure of various samples (Figure 3). For Ni/H−Al_2O_3 (Figure 3A-a), the peak in low temperature region (293 K) is attributed to CO desorption from weak binding sites of Ni (e.g., low index planes of Ni like Ni (111));[34−36] two desorption peaks in high temperature region attributed to CO (∼790 K) and CO_2 (∼805 K) are concomitantly observed, with the latter being strong and dominant. This indicates the abundant vacancy clusters of Ni, as strong binding sites, greatly promote dissociative adsorption of CO, followed by the conversion of most CO dissociatively adsorbed to CO_2 via the Boudouard reaction (eq S6) and the other fraction of CO dissociatively adsorbed desorbing as CO.[34−36] Compared with Ni/H−Al_2O_3, Ni_{A500}/H−Al_2O_3 (Figure 3A-b) and Ni_{A550}/H−Al_2O_3 (Figure 3A-c) show increased peak strength for molecular CO desorption in low temperature range but reduced desorption peaks of both CO_2 and CO in high temperature range. This indicates an increase in the weak binding sites (associated with flat surfaces of Ni) and a decrease in strong binding sites (Ni vacancy clusters) after the annealing treatment.

In order to give a better understanding on the influence of Ru clusters on the Ni surface structure, $Ru_{0.4}$−Ni/H−Al_2O_3 (Ru loading of 0.42 wt %) and $Ru_{2.5}$−Ni/H−Al_2O_3 (Ru loading of 2.5 wt %) were prepared, respectively, via the same synthesis method for $Ru_{0.8}$−Ni/H−Al_2O_3. Figure 3B shows the CO−TPD profiles of these three Ru−Ni samples and Ru/Al_2O_3. The peak centered at 417 K is assigned to molecular CO desorption from metal Ru in Ru/Al_2O_3 (Figure 3B-a). In the high temperature range, the desorption peaks of both CO_2 (∼810 K) and CO (∼780 K) for the three Ru−Ni samples drop obviously compared with Ni/H−Al_2O_3. This suggests the blocking of Ni vacancy clusters via Ru clusters and the subsequently restrained CO dissociation. Notably, in the low temperature range, besides the CO desorption from weak binding sites (∼300 K), an additional shoulder peak in 330−510 K is observed. This is likely attributed to the CO desorption from the Ru−Ni interfacial site and the Ru site. The TPD profiles can be further deconvoluted to three peaks in the temperature range 210−510 K, and the results are presented in Figure 3B and Table 2S. The three peaks at ∼300 K, ∼365 K, and ∼425 K are attributed to CO desorption from the weak binding site, the Ru−Ni interfacial site, and the Ru site, respectively. It is interesting that the desorption capacity from these three sites follows different rules along with the increase of Ru loading from 0.42 wt % to 2.5 wt %: the CO desorption from the Ni weak binding site reduces gradually, while the CO desorption from the Ru site enhances accordingly, as a result of the increased coverage of Ru clusters on the Ni surface. In the case of the CO desorption from the Ru−Ni interfacial site with a moderate binding strength, the desorption capacity increases first and then decreases, and the maximum desorption capacity is present in the sample of $Ru_{0.8}$−Ni/H−Al_2O_3. This indicates an optimal Ru loading (0.85 wt %) to maximize the amount of the Ru−Ni interfacial site.

DOI: 10.1021/acs.chemmater.6b01784
Chem. Mater. 2016, 28, 4751−4761

Table 3. Catalytic Performances of Various Samples for ESR[f]

catalyst	TOF_{C_1}[a] (h^{-1})	TOF_{CH_4}[b] (h^{-1})	TOF_{H_2}[c] (h^{-1})	Y_{H_2} (mol_{H_2}/mol_{EtOH})	X_{EtOH} (%)	S_{H_2} (%)	S_{CO_2} (%)	S_{CO} (%)	S_{CH_4} (%)	S_{C_2}[d] (%)
$Ni/H-Al_2O_3$	684.4	322.3	254.6	2.2	100	37.2	51.1	1.8	47.1	0
$Ni_{A500}/H-Al_2O_3$	595.3	227.5	311.3	2.6	94.4	45.7	48.9	5.1	33.4	12.6
$Ni_{A550}/H-Al_2O_3$	521.7	184.4	312.6	2.5	90.2	46.8	39.9	10.7	27.5	21.9
$Ru_{0.4}-Ni/H-Al_2O_3$	740.9	240.7	422.5	3.2	95.3	56.0	65.1	1.2	31.9	1.8
$Ru_{0.8}-Ni/H-Al_2O_3$	872.7	179.9	638.8	4.2	97.5	71.0	76.2	0.8	20.0	3.0
$Ru_{2.5}-Ni/H-Al_2O_3$	622.2	124.4	516.8	2.2	65.6	56.9	42.6	12.2	13.7	31.5
Ru/Al_2O_3	308.2	140.3	654.7[e]	0.9	50.6	30.8	4.2	3.7	6.6	85.5

[a]TOF_{C_1} (h^{-1}) denotes the turnover frequency of C_1 species production (described in the Supporting Information), which was calculated on the basis of effective conversion of ethanol (the conversion of ethanol to C_1 species) at surface metal atoms. [b]TOF_{CH_4} (h^{-1}) denotes the turnover frequency of CH_4 production (described in the Supporting Information), which reflects the efficiency of C−O bond cleavage and catalytic activity toward methanation. [c]TOF_{H_2} (h^{-1}) denotes the turnover frequency of H_2 production (described in the Supporting Information). [d]S_{C_2} represents the selectivity toward C_2 species including acetaldehyde and/or ethylene. [e]TOF_{H_2} of Ru/Al_2O_3 reflects the catalytic activity toward the ethanol dehydrogenation other than steam reforming to produce H_2. [f]350 °C, H_2O/EtOH = 6, WHSV: 10 h^{-1}.

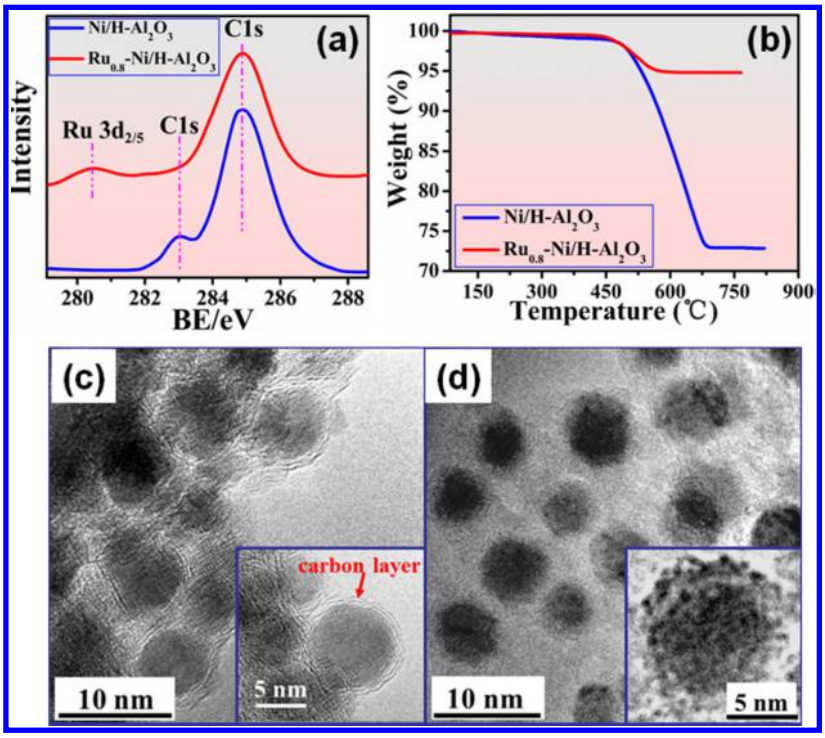

Figure 5. (a) XPS spectra of C 1s for $Ni/H-Al_2O_3$ and $Ru_{0.8}-Ni/H-Al_2O_3$ after used in ESR for 80 h; (b) TG curves for $Ni/H-Al_2O_3$ and $Ru_{0.8}-Ni/H-Al_2O_3$ after ESR reaction for 80 h; TEM images of (c) $Ni/H-Al_2O_3$ and (d) $Ru_{0.8}-Ni/H-Al_2O_3$ after used in ESR for 80 h.

The Catalytic Performances toward ESR. The ethanol steam reforming (ESR) process is composed of several possible reactions, depending on the reaction conditions and catalyst structure. The key challenge is the catalyst design and exploration so as to achieve a high yield of H_2 at mild reaction temperature. We tested the catalytic performances of the three Ni-based catalysts, three Ru−Ni catalysts, and Ru/Al_2O_3 toward ESR at a low temperature of 350 °C (Figure 4 and Table 3). The sample of Ru/Al_2O_3 shows a poor capability to break the C−C bond (C_1 species selectivity: 14.5%; TOF_{C_1}: 308.2 h^{-1}) but catalyzes the ethanol dehydrogenation to produce acetaldehyde and H_2 (acetaldehyde selectivity: 75.5%), as is well-known for Ru-based catalysts.[37] In contrast, $Ni/H-Al_2O_3$ with a high density of Ni vacancy clusters displays an outstanding activity to C−C bond cleavage (TOF_{C_1}: 684.4 h^{-1}). However, a very high methane selectivity (47.1%) and a relatively low H_2 selectivity (37.2%) are observed, suggesting the side reaction of methanation is largely promoted (TOF_{CH_4}: 322.3 h^{-1}). After the annealing treatment, for $Ni_{A500}/H-Al_2O_3$ and $Ni_{A550}/H-Al_2O_3$, the catalytic activities toward both C−C bond cleavage and methanation drop obviously (TOF_{C_1}: from 684.4 to 521.7 h^{-1}; TOF_{CH_4}: from 322.3 to 184.4 h^{-1}). Furthermore, the correlation between TOF_{CH_4} and the relative concentration of Ni surface vacancy clusters (I_2/I_1 ratio), and TOF_{C_1} as a function of I_2/I_1 ratio, show a linear relation, respectively (Figure 4b). This indicates that Ni vacancy clusters as active sites catalyze both C−C bond and C−O bond cleavage (as the rate-determining step for methanation) simultaneously. However, it should be noted that the intercept of the TOF_{CH_4} straight line is much smaller (0.779, rather close to zero at the zero vacancy clusters) compared with that of the

DOI: 10.1021/acs.chemmater.6b01784
Chem. Mater. 2016, 28, 4751−4761

TOF_{C_1} straight line (318.5), which suggests that the C−O bond breaking has a significantly stronger dependence on Ni vacancy clusters.

For the three Ru−Ni catalysts, by the blocking of Ni vacancy clusters via anchoring Ru clusters, methanation is obviously restrained (as shown in Figure 4a), indicating the inhibition of C−O bond breaking. With the increase of Ru loading, the TOF_{C_1} increases first and then decreases, and the maximum TOF_{C_1} (872.7 h^{-1}) is present in the sample of $Ru_{0.8}$−Ni/H−Al_2O_3. This is greatly larger than that of Ni/H−Al_2O_3 (684.4 h^{-1}). According to the highest amount of the Ru−Ni interfacial site in $Ru_{0.8}$−Ni/H−Al_2O_3 revealed by CO−TPD, it is concluded that the Ru−Ni interfacial site accounts for the largely enhanced TOF_{C_1}. Moreover, the strong correlation between TOF_{C_1} and the amount of the Ru−Ni interface site ($CO_{interface}$ desorption capacity) indicates that the Ru−Ni interface site as a new active center compensates the decrease in Ni vacancy clusters and effectively promotes the C−C bond cleavage (Figure 4c). To the best of our knowledge, $Ru_{0.8}$−Ni/H−Al_2O_3 in this work exhibits the highest TOF_{H_2} (638.8 h^{-1}) and H_2 yield (4.2 mol_{H_2}/mol_{EtOH}) compared with the previously reported ESR catalysts working at medium-low temperature (300−500 °C) (as shown in Table S3).

In situ FTIR confirms that the modification of Ru clusters to Ni/H−Al_2O_3 inhibits the methanation but promotes WGSR (the key intermediate reaction step for H_2 production), leading to a remarkable increase of the H_2 yield at 350 °C (see Figure S2 and corresponding discussion). In addition, the long-term catalytic stability of Ni/H−Al_2O_3 and $Ru_{0.8}$−Ni/H−Al_2O_3 are further investigated (Figure 4d). The $Ru_{0.8}$−Ni/H−Al_2O_3 maintains a stable H_2 yield, with a total decrease of 1.7% within 80 h; while the level of a H_2 yield over Ni/H−Al_2O_3 decreases quickly after 24 h, with a total drop of 25% within 80 h. XPS results (Figure 5a) show that for the used Ni/H−Al_2O_3, two C 1s signals (284.8 and 283.2 eV) are observed, which are attributed to the sp^2 carbon and C atoms in intimate contact with the metal (surface carbide),[38] respectively. However, the C electronic fingerprint (283.2 eV) is not found for the used $Ru_{0.8}$−Ni/H−Al_2O_3. The TGA test (Figure 5b) reveals that the used Ni/H−Al_2O_3 displays a much larger weight loss compared with the used $Ru_{0.8}$−Ni/H−Al_2O_3 (26.1% vs 4.9%), indicating a significant amount of carbon deposit on Ni/H−Al_2O_3. This is further illustrated by the TEM image. Figure 5c clearly shows a thick carbon coating on the Ni nanoparticles in the used Ni/H−Al_2O_3, but this is not detected in the used $Ru_{0.8}$−Ni/H−Al_2O_3 (Figure 5d). The results above demonstrate that the superimposition of Ni surface defects by Ru clusters effectively inhibits the surface carbon deposition and thus enhances the catalytic stability.

Study on the Property-Structure Correlation. To give deep insight into the active site structure, the d-band projected densities of states (PDOS) for Ni atom configuration on the Ni terrace (111), the Ni step (311), and the perimeter of the Ru−Ni interface were studied by DFT calculations (Figure 6 and Table S4), which are comparable to the catalyst structure confirmed by experimental findings. The position of the d-band center of a metal dominantly affects the extent of metal−adsorbate interactions: an upshift of the d-band center of metal, with the whole d-bands closer to the Fermi level, leads to a stronger reactivity and interaction strength with the adsorbate.[39,40] In Figure 6A and B, a-1 and a-2 represent Ni atoms

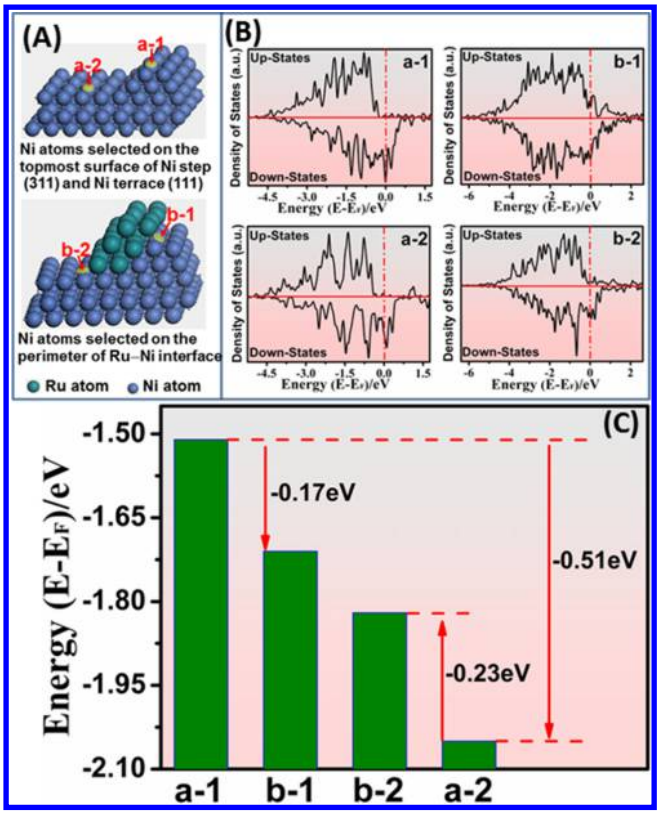

Figure 6. (A) Schematic illustration of the geometrical structures for the DFT-calculated d-band center of Ni atoms on the Ni terrace (111), the Ni step (311), and the perimeter of the Ru−Ni interface. (B) DFT-calculated d-band center of different Ni atoms selected from (A). (C) Variations in the d-band center energy of different Ni atoms selected from (A).

on the topmost surface of the Ni step (311) and the Ni terrace (111), respectively; b-1 and b-2 correspond to a-1 and a-2 sites after the anchoring of Ru clusters, which are located at the perimeter of the Ru−Ni interface. It is found that the a-1 site on step-edge displays a large upshift of the d-band center (0.51 eV) compared with the a-2 site on the terrace (−1.54 vs −2.05 eV) (Figure 6C), which can be attributed to the low-coordinated Ni atoms with a higher-lying d-band state. Since the d-band center of step-edge (at Ni step (311)) is much closer to the Fermi level, it shows much stronger bond-breaking activity (e.g., C−O and C−C bond cleavage) compared with the Ni terrace (111).[19,20,41−44] Therefore, the Ni vacancy clusters with step-edge sites in Ni/H−Al_2O_3 exhibit a strong capability to break C−C and C−O bonds simultaneously without a specific bond-breaking selectivity, resulting in a low H_2 selectivity in ESR. Moreover, owing to the large upshift of the d-band center, the Ni vacancy clusters are prone to show a strong binding of the intermediate product (e.g., CO, as shown in CO−TPD) and concomitantly reduced availability of active sites, accounting for the relatively low turnover frequency (e.g., TOF_{C_1}). In contrast, the d-band center of the Ni terrace (111) is rather far from the Fermi level, which results in a weak binding strength/interaction with adsorbate and is not conducive to activate reactants. This is in accordance with the results of catalytic evaluation and CO−TPD over annealed Ni/H−Al_2O_3.

After anchoring Ru clusters onto Ni, the b-1 site displays a downshift of the d-band center (0.17 eV) relative to the a-1 site

DOI: 10.1021/acs.chemmater.6b01784
Chem. Mater. 2016, 28, 4751−4761

(−1.71 vs −1.54 eV) (Figure 6C), which is ascribed to the formation of Ru−Ni coordination with reduced unsaturation degree of Ni on step sites. This indicates that the anchoring of Ru clusters as "ligand" changes the high energy state to a moderate energy state. In contrast, compared with the a-2 site with low energy (−2.05 eV), the b-2 site shows an upshift of the d-band center (0.23 eV) and reaches to a moderate position (−1.82 eV) (Figure 6C), which can be attributed to an electronic effect, namely, the strain effect at the Ru−Ni interface. As discussed above, a marked tensile/expansion of Ni lattice (as shown in Figure 1j−k) is observed at the interface. When Ni atoms at the interface are subjected to a tensile strain, the d-orbital overlap is decreased, resulting in an upshift of the d-band center.[43,45] As a result, due to the ensemble effect imposed by both "ligand" and tensile strain, the d-band center of Ni atoms at the Ru−Ni interface is tuned to a moderate position, leading to an intermediate-strength-binding with the adsorbate (e.g., CO, as shown in CO−TPD). This often results in a largely improved catalytic performance with the desired product/reaction route.[44,46]

Notably, in this work, it is found that the C−O bond cleavage shows a much stronger vacancy-clusters-dependence compared with C−C bond cleavage. Previous theoretical studies reported that C−O bond cleavage shows strong structural effects, which intensively requires a double step-edge site with a high-lying d-state;[18,20] the barrier for C−O bond cleavage is obviously higher than that for C−C cleavage.[47,48] This indicates that C−O bond cleavage requires a higher d-band-energy-state of active metal than C−C bond breaking. As a result, based on the desirable modulation of the metal d-band center position to a moderate energy state, the Ru−Ni interfacial sites as active sites substitute the original Ni surface defects, resulting in the inhibition of C−O breaking and the promotion of C−C bond cleavage. The calculation studies agree well with the experimental findings including structural properties and catalytic evaluation over $Ru_{0.8}$−Ni/H−Al_2O_3.

CONCLUSIONS

In summary, a Ru−Ni bimetallic catalyst is obtained by employing the surface defects of Ni nanoparticles as nucleation sites to induce the growth of Ru clusters. The resulting Ru−Ni/H−Al_2O_3 catalyst exhibits a high activity and a significantly enhanced H_2 yield toward ESR at low temperature (350 °C). Both the experimental studies and DFT calculations demonstrate that the conversion of Ni surface defects to the Ru−Ni interface plays a critical role in the bond-breaking selectivity between C−O and C−C bond. The decrease of Ni surface defects effectively inhibits C−O bond rupture and the subsequent side reaction of methanation; while the formation of the Ru−Ni interface with a moderate d-band center position facilitates the C−C bond cleavage and the resulting WGSR. Therefore, such studies on the bond-breaking selectivity via bimetallic interface modulation could become a powerful tool in the nanoscale design of new catalysts.

EXPERIMENTAL SECTION

Materials. Chemical reagents, including $Ni(NO_3)_2{\cdot}6H_2O$, $Al_2(SO_4)_3{\cdot}18H_2O$, urea [$CO(NH_2)_2$], sodium tartrate, $RuCl_3{\cdot}3H_2O$, $NH_3{\cdot}H_2O$, and NH_4NO_3, were obtained from Beijing Chemical Co., Ltd., and used without further purification. Deionized and decarbonated water was used in all the experimental processes.

Preparation of Ni/H−Al_2O_3 and Annealed Ni/H−Al_2O_3. First, the hierarchical NiAl−LDH microspheres (denoted as H−LDH) used as a precursor were synthesized by an in situ growth technique as described in our previous work.[21] The Ni/H−Al_2O_3 sample was obtained via an in situ reduction process of the H−LDH precursor. In a typical procedure, 0.8 g of H−LDH was reduced in a H_2/N_2 (60/40, v/v) stream at 450 °C for 4 h, with a heating rate of 5 °C/min. The reduction process results in the phase transformation from H−LDH to Ni/H−Al_2O_3 (Ni loading: ∼20 wt %), followed by fast cooling to the room temperature in a N_2 stream. For the preparation of annealed Ni/H−Al_2O_3, Ni/H−Al_2O_3 was further reduced in a H_2/N_2 (10/90, v/v) stream at different temperatures (500 or 550 °C) for 5 h, with a heating rate of 2 °C/min. The resulting product Ni_{A500}/H−Al_2O_3 or Ni_{A550}/H−Al_2O_3 was cooled very slowly to the room temperature in a N_2 stream.

Preparation of Ru−Ni/H−Al_2O_3. The sample of Ru−Ni/H−Al_2

stable condition in 3 h, and coking can be neglected during the reaction. The carbon balance with an error was within ±5% for all catalytic evaluation experiments. Notably, the sum of carbon-containing species selectivity (S_{C_i}) and H_2 selectivity (S_{H_2}) does not result in unity, since they are calculated on the basis of independent carbon and hydrogen balances, respectively.

Characterization. A FEI Tecnai F30 microscope operated at 300 kV was employed to conduct structural investigations of various catalysts by using TEM, HRTEM, and STEM mode. The elemental maps were obtained by using high-angle annular dark-field scanning TEM (HAADF-STEM) of energy-dispersive X-ray (EDX) mode. The specific surface area was determined by Brunauer−Emmett−Teller (BET) methods using a Quantachrome Autosorb-1C-VP analyzer. Positron annihilation measurements were performed with a fast−slow coincidence ORTEC system with a time resolution of 187 ps for the full width at half-maximum. A 5 × 105 Bq source of ^{22}Na was sandwiched between two identical samples. The electronic and chemical environment of the positron trapping center are usually identified by the parameters S and W obtained from coincidence Doppler broadening (CDB) of positron annihilation spectroscopy, the values of which reflect the relative contributions to positron annihilation of the lower- and higher-momentum electrons, respectively. Coincidence Doppler broadening (CDB) collected the energy range of total peak for gamma energy spectrum from 503.34 to 518.88 keV; the S parameter is defined as the ratio between energy count within 510.24−511.76 keV and energy count of total peak (503.34.2−518.88 keV); the W parameter is defined as the ratio between energy count within 514.83−518.66 keV and 503.34−507.17 keV and energy count of total peak (503.34.2−518.88 keV). The extended X-ray absorption fine structure (EXAFS) spectroscopy was measured at beamline 1W1B of the Beijing Synchrotron Radiation Facility (BSRF), Institute of High Energy Physics (IHEP), Chinese Academy of Sciences (CAS). The typical energy of the storage ring was 2.5 GeV with a maximum current of 250 mA; the Si (111) double crystal monochromator was used. Fourier transform of the EXAFS spectra was carried out in a K-range from 3.0 to 12.8 $Å^{-1}$. The IFFEFIT 1.2.11 date analysis package (Athena, Artemis, Atoms, and FEFF6) was used for the date analysis and fitting. Elemental analysis for Ni and Ru was performed using a Shimadzu ICPS-7500 inductively coupled plasma−atomic emission spectrometer (ICP−AES). CO−TPD measurements were conducted in a quartz tube reactor on a Micromeritics Auto Chem II 2920 instrument with an online mass spectrometry (MS). In a typical process, 100 mg of sample was first reduced at 400 °C for 1 h in 10 vol % H_2/Ar, followed by flushing (50 mL/min) with high purity He for 0.5 h at 400 °C. Afterward, as the temperature decreased to 200 K, successive pulses of CO were injected, using He (50 mL/min) as the carrier gas, until a stable mass signal for CO was obtained. Subsequently, the TPD process was carried out up to 900 °C at a rate of 10 °C/min, by using high purity He as the carrier gas (50 mL/min). *In situ* FTIR patterns were recorded for Ni/H−Al_2O_3 and $Ru_{0.8}$−Ni/H−Al_2O_3 in a WGSR environment using a Vertex 70 (Bruker) spectrophotometer with a modified transmission FTIR cell connected to a gas flow system. The sample (50 mg) was pressed into a disk and activated in 10% H_2/He at 400 °C for 1 h. The input gas with 1% CO plus 3% H_2O in He was fed into the FTIR cell. Stepwise heating was used, and the temperature was kept for 1 h at each following step during heating: 100, 200, 250, 300, and 350 °C, respectively.

Computational Methods.

(50) Perdew, J. P.; Burke, K.; Ernzerhof, M. Generalized gradient approximation made simple. Phys. Rev. Lett. 1996, 77, 3865−3869.

DOI: 10.1021/acs.chemmater.6b01784
Chem. Mater. 2016, 28, 4751−4761